J Supercond Nov Magn (2011) 24:1947–1956
DOI 10.1007/s10948-011-1150-4

ORIGINAL PAPER

Mechanical Properties of $(Cu_{0.5}Tl_{0.5})$-1223 Substituted by Pr

R. Awad · A.I. Abou Aly · M. Kamal · M. Anas

Received: 4 January 2011 / Accepted: 14 February 2011 / Published online: 16 March 2011

Abstract $Cu_{0.5}Tl_{0.5}Ba_2Ca_{2-x}Pr_xCu_3O_{10-\delta}$ superconducting samples, with $0 \leq x \leq 0.15$, were prepared by a single-step solid state reaction on a form of rectangular bar. The prepared samples were characterized using X-ray powder diffraction (XRD) and scanning electron microscope (SEM). The room temperature Vickers microhardness was measured at different loads (0.25–3 N). The experimental results were analyzed using Meyer's law, Hays–Kendall approach, elastic/plastic deformation model, proportional specimen resistance model, and the indentation-induced cracking (IIC) model. Surprising results were obtained and showed that all samples in the form of rectangular bars exhibited reverse indentation size effect in contrary with those in the form of discs. Vickers microhardness values were decreased as Pr-content increased that consisting with the porosity results. Furthermore, the Young's modulus was determined using the dynamic resonance technique. A relation between Young's modulus (E) and Vickers microhardness (H_V) was obtained.

Keywords $(Cu_{0.5}Tl_{0.5})$-1223 · Vickers microhardness · Young's modulus · Pr-substitution

R. Awad (✉) · A.I. Abou Aly · M. Anas
Physics Department, Faculty of Science, Alexandria University, Alexandria, Egypt
e-mail: rawad64@yahoo.com

M. Kamal
Physics Department, Faculty of Science, Mansoura University, Mansoura, Egypt

1 Introduction

Mechanical properties of high-temperature superconductors, HTSCs, are intimately connected with their physical properties. They determine the performance of devices prepared from it. Consequently, it is important for assessing the mechanical properties of HTSCs. Among the various experimental techniques, for determining the mechanical properties, microhardness testing is frequently used to assess the mechanical properties of solids in the form of bulk samples and thin films.

Vickers microhardness test is one of the convenient methods to estimate the mechanical properties of materials. Vickers microhardness test was applied to different kind of materials (superconductors, ceramics, semiconductors, thin films, polymers and alloys) [1–7]. Terzioglu et al. [8] investigated the effect of annealing temperature on the mechanical properties of MgB_2 superconductor. They found that the Vickers microhardness of these samples was dependent on the annealing temperature and the applied load. The maximum Vickers microhardness (H_V) of 3.824 GPa was obtained at annealing temperature of 850 °C and load 0.245 N. Kolemen et al. [3] studied the effect of Sm-substitution on the Vickers microhardness of $Bi_{1.6}Pb_{0.4}Sr_2Ca_{2-x}Sm_xCu_3O_{10-\delta}$ with $x = 0.0$, 0.001, 0.005 and 0.1. They showed that Kick's law failed to explain the variation in the Vickers microhardness with applied load. Whereas the modified proportional specimen resistance (PSR) model was more suitable than Hays–Kendall approach to estimate the load independent Vickers microhardness of these samples for loads greater than 1.0 N. Cetinkara et al. [9] studied the influence of cooling rate on the mechanical properties of $Bi_{1.6}Pb_{0.4}Sr_2Ca_2Cu_3O_{10-\delta}$ superconductor. They found that the mechanical properties of the prepared samples were dependent on the load and

the cooling rate. The effect of Gd-addition on the mechanical properties of $Bi_{1.8}Pb_{0.35}$ $Sr_{1.9}Ca_{2.1}Cu_3Gd_xO_{10-\delta}$, with $0 \leq x \leq 0.4$, was studied by Aydin et al. [10]. The results showed that Gd-addition degraded the mechanical properties due to increase in voids, an impurity phase, and resistance to crack propagation. Leenders et al. [11] investigated the influence of thermal cycling on the mechanical properties of vertical gradient freeze (VGF) melt-textured YBCO. They showed that the Vickers microhardness was found to be load dependent. On the other hand, the thermal cycling changed the measured Vickers microhardness but did not affect the true Vickers microhardness. Mohammed et al. [12] studied the effect of nano-SnO_2 addition on the mechanical properties of $(Cu_{0.5}Tl_{0.5})$-1223. Their results showed that the samples had normal indentation effect. Moreover, the addition of nano-SnO_2 resulted in an increase of Vickers microhardness and Young's modulus. The comparison between the effect of nano-SnO_2 and nano-In_2O_3 addition on $(Cu_{0.5}Tl_{0.5})$-1223 was studied by Mohamed et al. [13]. The results showed that the addition of nano-SnO_2 up to $x = 1$ wt.% improved the mechanical properties of $(Cu_{0.5}Tl_{0.5})$-1223, while only low addition of nano-In_2O_3, $x = 0.1$ wt.%, enhanced the microhardness of the phase. Furthermore, the values of Young's modulus, yield strength, fracture toughness and brittleness index for $(Cu_{0.5}Tl_{0.5})$-1223 added by nano-SnO_2 were found to be much higher than those for $(Cu_{0.5}Tl_{0.5})$-1223 added by nano-In_2O_3.

The determination of Young's modulus of different types of HTSCs was done by many authors [11, 14–19]. Most of them used an empirical formula [20] to estimate Young's modulus from the Vickers microhardness. This formula was based on the measurements of $Bi_{2-x}Pb_xSr_2Ca_2Cu_3O_{10-\delta}$ superconductors [20]. In this work, we try to obtain the best fit relation between Vickers microhardness and Young's modulus for $(Cu_{0.5}Tl_{0.5})$-1223 system. For this purpose, superconducting samples of type $Cu_{0.5}Tl_{0.5}Ba_2Ca_{2-x}Pr_xCu_3O_{10-\delta}$, with $0 \leq x \leq 0.15$, were prepared by a single-step solid state reaction technique and characterized by EDX and SEM. Furthermore, the Vickers microhardness and Young's modulus were measured at room temperature using Vickers tester and dynamic resonance technique, respectively.

2 Experimental Technique

Superconducting samples of the nominal compositions $Cu_{0.5}Tl_{0.5}Ba_2Ca_{2-x}Pr_x$ $Cu_3O_{10-\delta}$, with $x = 0.00$, 0.025, 0.05, 0.075, 0.10 and 0.15,were prepared by a single-step solid state reaction technique. High purity starting oxides of Tl_2O_3, BaO_2, CaO, Pr_6O_{11}, and CuO taken in stoichiometric ratios 0.6:2:2-x: x: 3.5 were grind in agate mortar and sifted twice by a 65 μm sieve. The powder was pressed, to a pressure of 15 Tons/inch^2 using a hydrostatic press, on form of rectangular bar of dimensions $5 \times 0.3 \times 0.2$ cm^3. The samples were then wrapped in a silver foil to minimize the thallium losses during the sintering process. The samples were heated in a sealed quartz tube (2 cm diameter and 12 cm long) at a rate of 4 °C/min up to 760 °C, followed by heating rate of 2 °C/min up to 850 °C, and held at this temperature for 5 hours. At the end of this step, the samples were slowly cooled to room temperature by a rate of 2 °C/min.

The samples were characterized by X-ray powder diffraction (XRD) using Shimadzu-7000 with Cu K_α-radiation ($\lambda = 1.5418$ Å) in the range $3° \leq 2\theta \leq 70°$. The grain size and microstructure morphology of the samples were identified using Jeol scanning electron microscope JSM-5300, operated at 25 kV, with a resolution power of 4 nm. Vickers microhardness measurements of the studied samples were performed in atmospheric air using a digital Vickers microhardness tester FM-7 at room temperature. The applied load was varied from 0.25 to 3 N for a loading time of 10 seconds, and the diagonals of indentation were measured with an accuracy of ±0.1 μm. An average value of the Vickers microhardness, for each load, was calculated by taking five readings at different locations on the specimen surface. The Vickers microhardness is calculated from the relation [11]:

$$H_V = 1854.4\frac{F}{d^2} \quad \text{GPa}, \tag{1}$$

where F is the applied load in Newton (N), and d is the diagonal length in μm.

The Young's modulus of some selected samples were measured at room temperature using a hand made apparatus based on dynamic resonance technique as shown in Fig. 1. Determination of Young's modulus (E) by the dynamic method is based on measurement of the density, geometrical dimensions, and frequency of natural oscillations (f_0) of bar specimens. In the presence of longitudinal oscillations of a bar specimen with a constant right-angled cross section with free ends, the Young's modulus is determined from the relation [21–23]:

$$E = \frac{38.32\rho L^4 f_0^2}{t^2}, \tag{2}$$

where ρ, L, and t are the density, length, and thickness of the measured sample, respectively.

3 Results and Discussion

3.1 Sample Characterization

X-ray diffraction patterns for $Cu_{0.5}Tl_{0.5}Ba_2Ca_{2-x}Pr_x$ $Cu_3O_{10-\delta}$ samples, with $0.0 \leq x \leq 0.15$ are shown in Fig. 2.

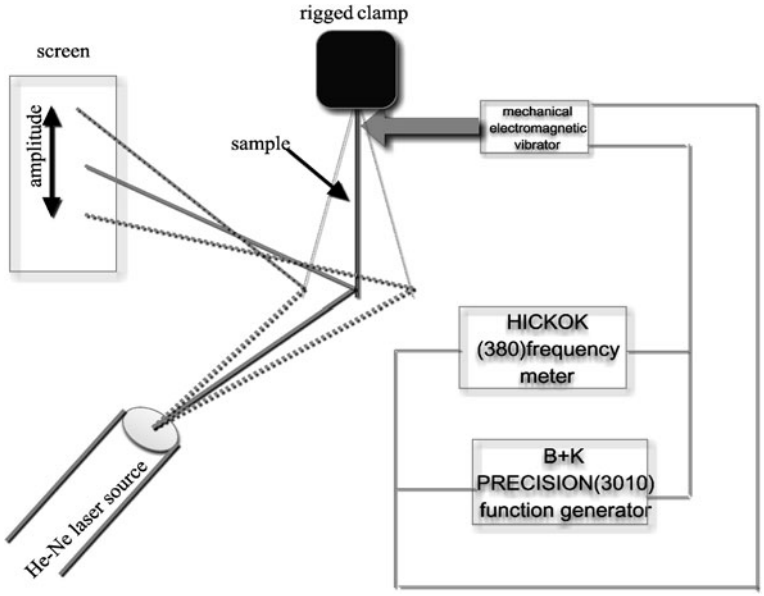

Fig. 1 Experimental setup of the dynamic resonance technique

Table 1 The volume fractions of $(Cu_{0.5}Tl_{0.5})$-1223, $(Cu_{0.5}Tl_{0.5})$-1212, and BaCuO as well as the lattice parameters a and c estimated from XRD for $Cu_{0.5}Tl_{0.5}Ba_2Ca_{2-x}Pr_xCu_3O_{10-\delta}$ with Pr-content

x	$(Cu_{0.5}Tl_{0.5})$-1223 %	$(Cu_{0.5}Tl_{0.5})$-1212 %	$BaCuO_2$ %	a (Å)	c (Å)
0	86.2	6.2	7.6	3.850 (8)	15.905 (4)
0.025	89	3.7	7.3	3.849 (1)	15.938 (5)
0.05	84.8	8.7	6.5	3.848 (6)	15.964 (8)
0.075	81.6	10.9	7.5	3.847 (3)	16.025 (2)
0.1	76.8	15	8.2	3.845 (8)	16.106 (5)
0.15	63.5	25.3	11.2	3.844 (1)	16.255 (5)

Most of the diffraction peaks are well indexed by a tetragonal structure with the space group P4/mmm, indicating that the dominant phase in all prepared samples is $(Cu_{0.5}Tl_{0.5})$-1223. In addition, few weak diffraction peaks corresponds to $(Cu_{0.5}Tl_{0.5})$-1212 phase, typically found in the $(Cu_{0.5}Tl_{0.5})$-1223 phase prepared by solid-state reaction technique due to its low formation temperature [24]. Also, few small peaks of the nonsuperconducting $BaCuO_2$ phase are indexed. The volume fractions of these phases are calculated and listed in Table 1. The volume fraction of $(Cu_{0.5}Tl_{0.5})$-1223 phase increases as Pr-content increases up to $x = 0.025$, then it decreases as Pr-content increases. This means that low-content of Pr stabilizes the $(Cu_{0.5}Tl_{0.5})$-1223 phase, while the high-content reduces the formation of the $(Cu_{0.5}Tl_{0.5})$-1223 phase and enhances the formation of the $(Cu_{0.5}Tl_{0.5})$-1212 phase.

The lattice parameters a and c, for all prepared samples, were calculated by least square method from the knowledge of the Miller indices (hkl) and the interplanar distance d. The calculated values are listed in Table 1. A systematic increase in the lattice parameter c is observed with increasing of Pr-content in the final compound, while a decrease in the lattice parameter a is noticed. This behavior is expected because the ionic radius of Pr^{3+} ion (1.13 Å) is slightly larger than that of Ca^{2+} ion (1.12 Å). This is a direct evidence for increasing the bond lengths and decreasing the interplane couplings.

SEM micrographs for $Cu_{0.5}Tl_{0.5}Ba_2Ca_2Cu_3O_{10-\delta}$, $Cu_{0.5}Tl_{0.5}Ba_2Ca_{1.975}Pr_{0.025}Cu_3O_{10-\delta}$, and $Cu_{0.5}Tl_{0.5}Ba_2Ca_{1.85}Pr_{0.15}Cu_3O_{10-\delta}$ are shown in Figs. 3a, b, and c, respectively. The images for $x = 0.0$ and 0.025 show more regular plate-like grains and less irregular or spherical grains than that for $x = 0.15$. The regular plate-like grains indicate the presence of $(Cu_{0.5}Tl_{0.5})$-1223 phase, whereas the irregular shaped and spherical grains represent impurity phases such as $(Cu_{0.5}Tl_{0.5})$-1212 and $BaCuO_2$, respectively. It is observed that the number of irregular shaped and spherical grains decrease in the sample with $x = 0.025$, indicating that this sample is of the highest volume fraction of $(Cu_{0.5}Tl_{0.5})$-1223 phase. Although the grain size looks larger for $x = 0.0$ than that for $x = 0.025$, the volume fraction is larger for smaller grain size. The increase in the number of irregular shaped and spherical grains for $x = 0.15$ samples indicates the lower volume fraction of this sample. These results are consistent with those obtained from X-ray data which show that the sample with $x = 0.025$ has the highest volume fraction of $(Cu_{0.5}Tl_{0.5})$-1223 phase.

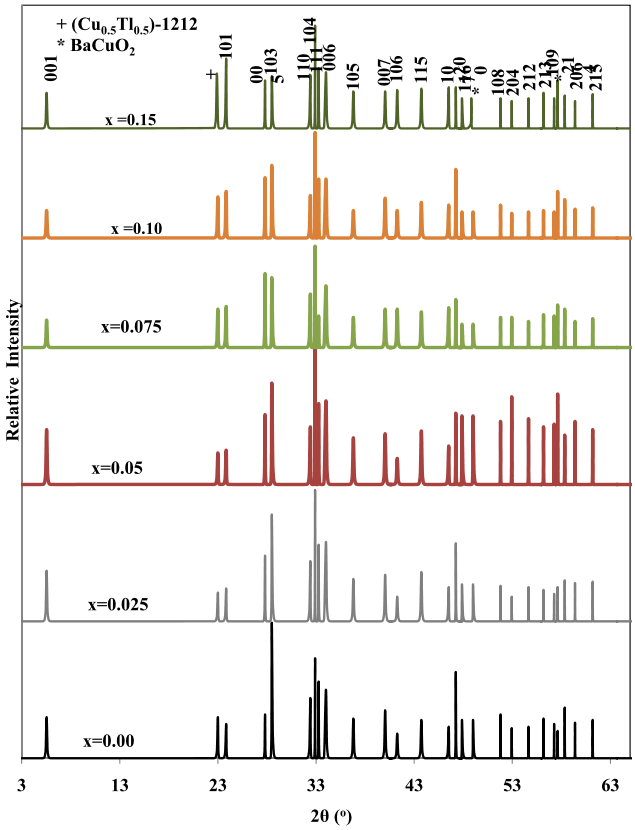

Fig. 2 XRD patterns for $Cu_{0.5}Tl_{0.5}Ba_2Ca_{2-x}Pr_xCu_3O_{10-\delta}$, with $0 \leq x \leq 0.15$

The porosity of these samples was calculated using the relation:

$$P = \left[1 - \frac{\rho_{\text{exp.}}}{\rho_{\text{theo.}}}\right] \times 100\%, \tag{3}$$

where $\rho_{\text{exp.}}$ and $\rho_{\text{theo.}}$ are the experimental and theoretical densities, respectively. The results show that the porosity increases as the Pr-content increases as shown in Fig. 4. The increasing of porosity with Pr-content can be observed from the SEM micrographs, where the density of voids increases as the Pr-content increases.

3.2 Vickers Microhardness Measurements

The superconductivity of the samples studied in this work was investigated through electrical resistivity measurements and the data showed that the superconducting transition temperature increased from 107.4 K to 124.3 K as x increased from 0 to 0.025 and then it decreased with further increase in x [25].

The Vickers microhardness H_V was calculated according to (1), and plotted as a function of the applied load for $Cu_{0.5}Tl_{0.5}Ba_2Ca_{2-x}Pr_xO_{10-\delta}$ $(0 \leq x \leq 0.15)$ in Fig. 5a. H_V increases rapidly as the applied load increases up to

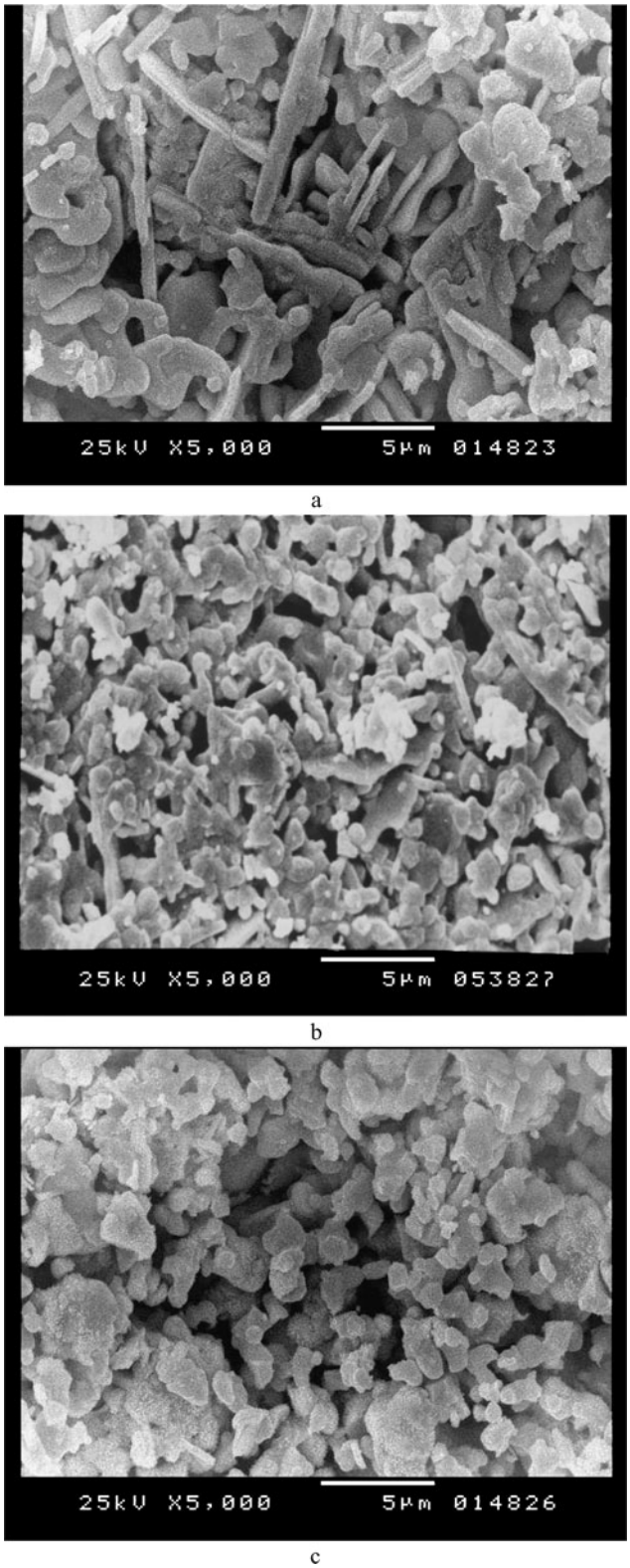

Fig. 3 SEM micrographs for (**a**) $Cu_{0.5}Tl_{0.5}Ba_2Ca_2Cu_3O_{10-\delta}$, (**b**) $Cu_{0.5}Tl_{0.5}Ba_2Ca_{1.975}Pr_{0.025}O_{10-\delta}$ and (**c**) $Cu_{0.5}Tl_{0.5}Ba_2Ca_{1.85}Pr_{0.15}O_{10-\delta}$

1.00 N, then it tends to attain saturation (nearly plateau) for higher loads (>1.00 N). This behavior was explained by Foerster et al. [26] on the basis of the penetration depth of the indenter. At small loads, the indenter affects only surface layers and surface effect dominates, while at higher loads the depth of penetration increases and the effect of inner layers becomes more prominent and ultimately there is no change in the microhardness values with increasing the applied load. This nonlinear behavior was also reported in many literatures [9–13, 19, 20] and it is known as the indentation size effect (ISE). As seen, all samples exhibit a reverse ISE, i.e., H_V increases with increasing the applied load. The dependence of the Vickers microhardness of $Cu_{0.5}Tl_{0.5}Ba_2Ca_{2-x}Pr_xCu_3O_{10-\delta}$ samples on the Pr-content is shown in Fig. 5b. A decrease of Vickers microhardness as Pr-content increases is observed. This behavior may be attributed to the increasing of density of voids and the low resistance to crack propagation with increasing the Pr-content. The decrease of the measured Vickers microhardness with increasing of substitution content is quite similar to that obtained by Aydin et al. [10] in $Bi_{1.8}Pb_{0.35}Sr_{1.9}Ca_{2.1}Cu_3Gd_xO_y$ phase. They attributed this behavior to the formation of impurity phases and irregularities, which is mainly distributed at the grain boundaries. These impurities and irregularities cause distortion in the bond strength, and consequently the microhardness values decrease [20]. These results are confirmed by the increase of porosity as Pr-content increases (see Fig. 4). The dependence of Vickers microhardness on porosity was reported in many literatures [27–29].

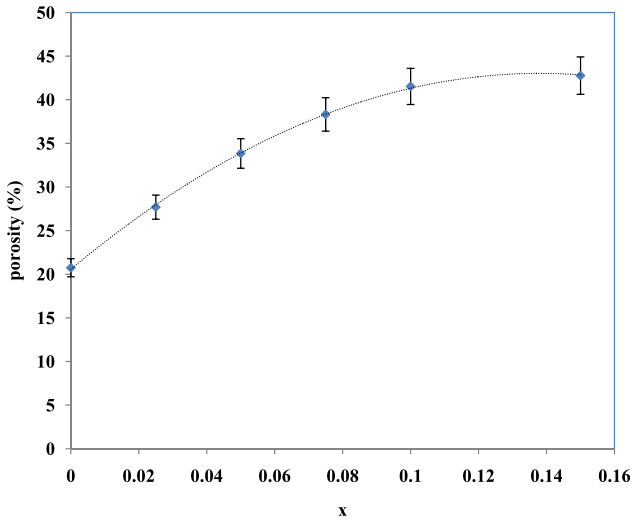

Fig. 4 Variation of porosity with x for $Cu_{0.5}Tl_{0.5}Ba_2Ca_{2-x}Pr_xCu_3O_{10-\delta}$ with $0 \le x \le 0.15$

In order to describe the ISE behavior of the samples studied, several relationships between the applied load and the indentation diagonal length are discussed in the following.

3.2.1 *Meyer's Law*

The simplest way to describe the ISE is Meyer's law [30–36] and the applied load is related to the indentation size d according to the formula:

$$F = Ad^n, \tag{4}$$

where A is a constant and it represents the load needed to initiate unit indentation. The exponent n is called Meyer's index which describe the ISE. The value of n is less than 2 for normal ISE, $n < 2$, while for reverse ISE the value of

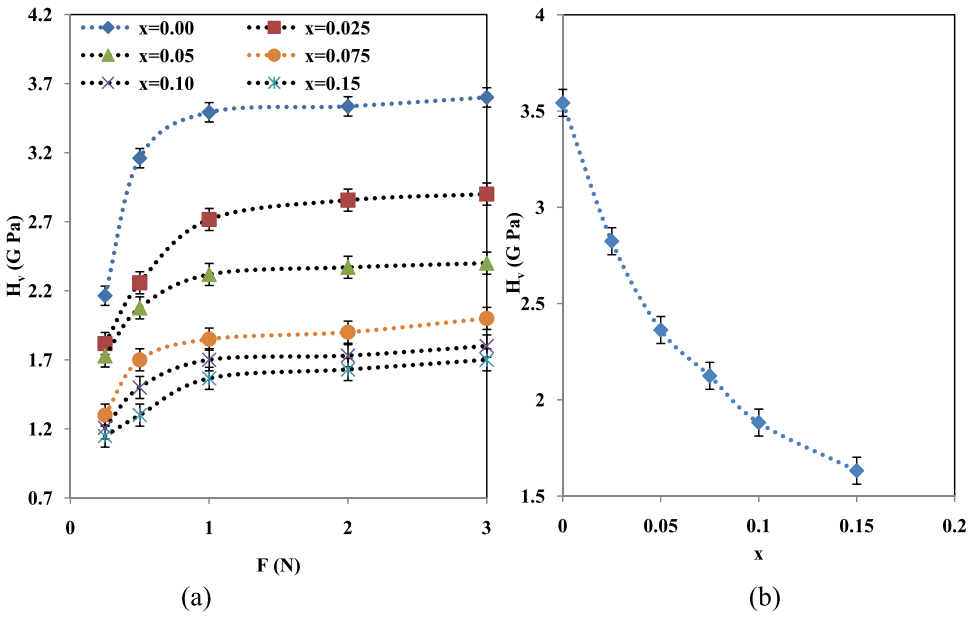

Fig. 5 (**a**) The dependence of Vickers microhardness H_V on the applied load F for $Cu_{0.5}Tl_{0.5}Ba_2Ca_{2-x}Pr_xCu_3O_{10-\delta}$ with $0 \le x \le 0.15$. (**b**) The dependence of Vickers microhardness H_V on x for $Cu_{0.5}Tl_{0.5}Ba_2Ca_{2-x}Pr_xCu_3O_{10-\delta}$ with $0 \le x \le 0.15$

Table 2 The calculated parameters according to different models for $Cu_{0.5}Tl_{0.5}Ba_2Ca_{2-x}Pr_xCu_3O_{10-\delta}$

x	Mayer's law		Hays–Kendall model		Elastic/Plastic deformation model		Proportional specimen resistance model		Indentation-induced cracking (IIC) model	
	n	$A \times 10^{-4}$ (N/μm^2)	$A_1 \times 10^{-3}$ (N/μm^2)	w (N)	$A_2 \times 10^{-3}$ (N/μm^2)	d_0 (μm)	$\alpha \times 10^{-2}$ (N/μm)	$\beta \times 10^{-3}$ (N/μm^2)	$K \times 10^5$ (N$^{(3-5m)/3}$/mm$^{(2-3m)}$)	m
0	2.52	3.33	2.00	−0.13	2.50	−3.68	−1.40	2.00	2.94	0.47
0.025	2.56	2.20	1.91	−0.17	2.02	−4.80	−1.50	1.89	2.18	0.45
0.05	2.53	2.13	1.80	−0.13	1.68	−4.46	−1.20	1.72	1.20	0.40
0.075	2.40	2.33	1.59	−0.11	1.22	−4.14	−0.80	1.63	1.53	0.43
0.1	2.63	1.32	1.40	−0.11	1.15	−4.35	−0.80	1.50	1.35	0.42
0.15	2.43	1.74	1.20	−0.14	1.09	−5.18	−0.90	1.31	1.27	0.42

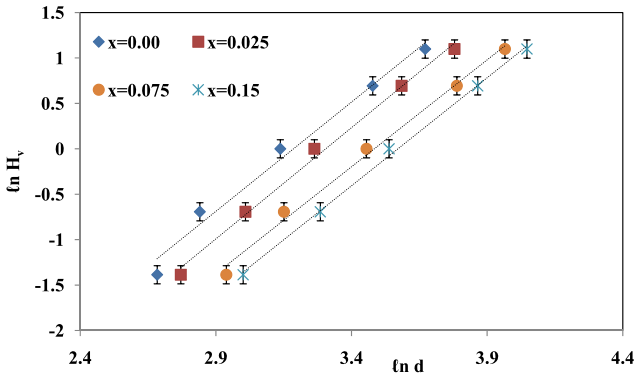

Fig. 6 Variation of $\ln H_V$ with $\ln d$ for $Cu_{0.5}Tl_{0.5}Ba_2Ca_{2-x}Pr_xCu_3O_{10-\delta}$ with $x = 0.00$, 0.025, 0.075 and 0.15

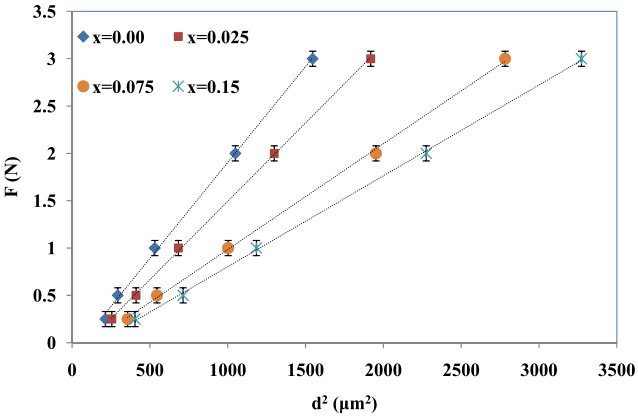

Fig. 7 Variation of the applied load with d^2 according to Hays–Kendall approach for $Cu_{0.5}Tl_{0.5}Ba_2Ca_{2-x}Pr_xCu_3O_{10-\delta}$ with $x = 0.00$, 0.025, 0.075 and 0.15

n is greater than 2, $n > 2$. When $n = 2$, H_V is independent of the applied load. Figure 6 shows typical plots of the dependence of $\ln F$ on $\ln d$ for some examined samples and the analysis of our experimental data according to (4) are listed in Table 2. It is obvious from Table 2 that all prepared samples have $n > 2$, indicating a reverse ISE behavior. It is clear that the calculated values of A are very small to be acceptable for ceramic materials which need higher loads to initiate indentation due to its hard nature.

3.2.2 Hays–Kendall Approach

Hayes and Kendall [37] proposed that there is a minimum test load w which is necessary to initiate plastic deformation and below it only elastic deformation occurs. Hence, the load dependence of indentation size is expressed as

$$F = w + A_1 d^2, \tag{5}$$

where A_1 is a constant independent of applied load. The values of w and A_1 can be calculated for some selected samples by plotting F against d^2 as shown in Fig. 7.

The calculated values of Hays–Kendall parameters are summarized in Table 2. It is noted that the values of w are negative for all examined samples, suggesting that the applied loads were large enough to create plastic deformation. The elastic deformation has not been observed in our work since the minimum load has been used was 0.025 N, which is sufficient to create plastic deformation in our samples.

3.2.3 Elastic/Plastic Deformation Model

According to Bull et al. [32, 38], the load dependence of indentation size is given by

$$F = A_2(d + d_0)^2, \tag{6}$$

where A_2 is a constant and d_0 is the correction in d due to a blunt indenter tip and elastic recovery associated with new bands of plastic deformation. A_2 and d_0 can be calculated by plotting $F^{1/2}$ against d as shown in Fig. 8 for $Cu_{0.5}Tl_{0.5}Ba_2Ca_{2-x}Pr_xCu_3O_{10-\delta}$ ($x = 0.00$, 0.025, 0.075 and 0.15). The calculated values of A_2 and d_0 are given in Table 2.

It is clear that the values of d_0 are negative which support that no elastic deformation is observed at this range of

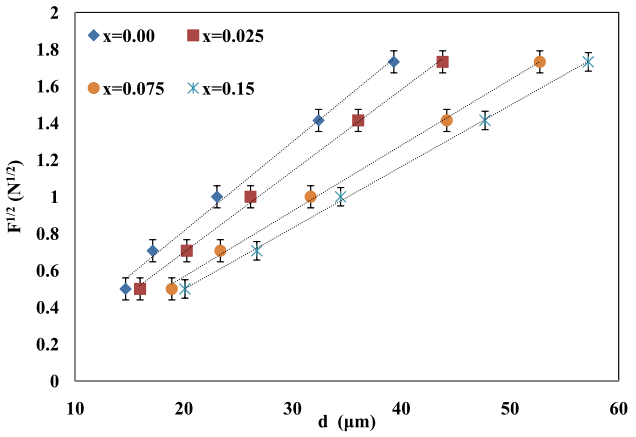

Fig. 8 Plot of $F^{1/2}$ vs. d according to Elastic/Plastic deformation model for $Cu_{0.5}Tl_{0.5}Ba_2Ca_{2-x}Pr_xCu_3O_{10-\delta}$ with $x = 0.00$, 0.025, 0.075 and 0.15

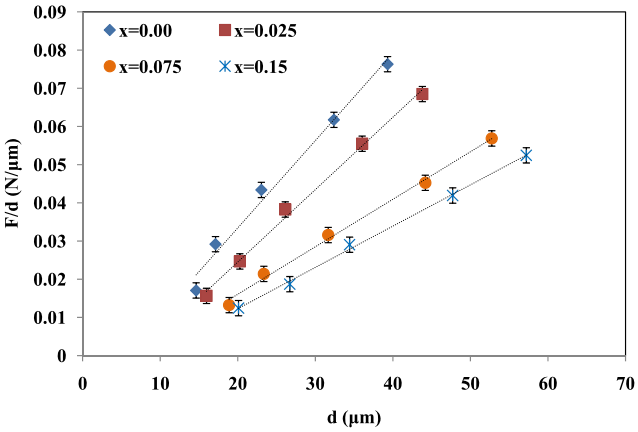

Fig. 9 Plot of F/d vs. d according to Proportional specimen resistance model for $Cu_{0.5}Tl_{0.5}Ba_2Ca_{2-x}Pr_xCu_3O_{10-\delta}$ with $x = 0.00$, 0.025, 0.075 and 0.15

applied loads for the examined samples. Moreover, the constant A_2 decreases as the Pr-content increases, confirming the decreasing of H_V with further increase in x.

3.2.4 *Proportional Specimen Resistance (PSR) Model*

According to several authors [33, 39–42], the ISE may be described by the relation:

$$F = \alpha d + \beta d^2, \tag{7}$$

where the parameter α characterizes the load dependence of the Vickers microhardness. The term αd is attributed to the specimen surface energy [40, 42], the deformed surface layer [43, 44], the indenter edges acting as plastic hinges [38], and the proportional specimen resistance [33, 34]. Li and Bradt [33] pointed out that the constants α and β of (7) are related with the elastic and plastic properties of the material, respectively. Moreover, they suggested that the constant α consists of two components; the first one is the elastic resistance of the test specimen, whereas the second one is the friction resistance developed at the indenter facet/specimen interface. Equation (7) can be rearranged as

$$F/d = \alpha + \beta d,$$

which enables to calculate α and β from the plots of F/d against d as shown in Fig. 9. The calculated values of both α and β are displayed in Table 2. As seen from the table, the values of α for all samples are negative in consistence with the results obtained from Hays–Kendall approach, where the term αd in the PSR model is equivalent to the constant w in Hays–Kendall approach. This fact confirms the absence of elastic deformation in the studied samples. Moreover, the constant β is suggested to be a measure of the so called "true hardness." It is noted that β decreases with the increasing of the Pr-content in agreement with the decreasing of the measured H_V as Pr-content increases as shown in the inset of Fig. 5.

3.2.5 *Indentation-Induced Cracking (IIC) Model*

The reverse ISE can be described by Li and Bradt [45]. They considered that, at the point of maximum penetration during the loading half-cycle, the applied indentation test load is balanced by the total specimen resistance composed of four components: friction at the indenter facet/specimen interface (frictional component), elastic deformation, plastic deformation, and specimen cracking. The first three components lead to the normal ISE, while the last one contributes to the reverse ISE. In the case of indentation cracking, the apparent Vickers microhardness measured by a Vickers diamond indenter may be given by

$$H_V = \lambda_1 K_1 \left(\frac{F}{d^2}\right) + K_2 \left(\frac{F^{5/3}}{d^3}\right), \tag{8}$$

where λ_1, K_1 and K_2 are constants. The constant K_2 depends on the applied load F while K_1 is a geometrical conversion factor whose value depends on the indenter geometry. For an ideally perfect plastic body, $H_V = K_1(F/d^2)$, $\lambda_1 = 1$, and $K_2(F^{5/3}/d^3) = 0$. In the case of a perfect brittle solid, $H_V = K_2(F^{5/3}/d^3)$ and $\lambda_1 = 0$. In (8), the indentation diagonal is assumed to be $d = 7h$, where h is the indentation depth. The applicability of (8) is to examine the H_V data by taking only the second term of this equation. Then (8) can be written as follows:

$$H_V = K \left(\frac{F^{5/3}}{d^3}\right)^m, \tag{9}$$

where K and the exponent m are constants that are load independent. Figure 10a shows the dependence of $\ln(H_V)$ on

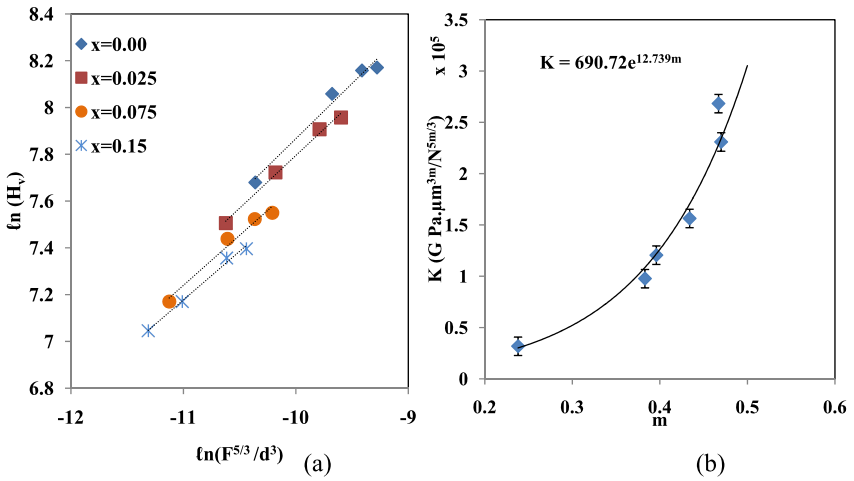

Fig. 10 (**a**) Variation of ln H_V with ln $(F^{5/3}/d^3)$ according to IIC model for $Cu_{0.5}Tl_{0.5}Ba_2Ca_{2-x}Pr_xCu_3O_{10-\delta}$ with $x = 0.00$, 0.025, 0.075, and 0.15. (**b**) The correlation between the IIC model parameters K and m for $Cu_{0.5}Tl_{0.5}Ba_2Ca_{2-x}Pr_xCu_3O_{10-\delta}$ with $0 \leq x \leq 0.15$

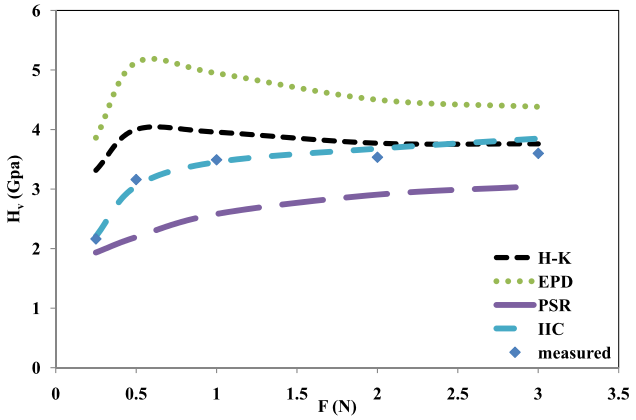

Fig. 11 Variation of the measured H_V and calculated H_V according to different models with the applied load for $Cu_{0.5}Tl_{0.5}Ba_2Ca_2Cu_3O_{10-\delta}$

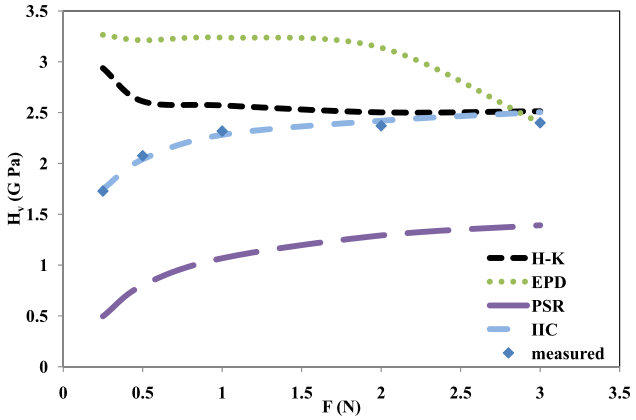

Fig. 12 Variation of the measured H_V and calculated H_V according to different models with the applied load for $Cu_{0.5}Tl_{0.5}Ba_2Ca_{1.95}Pr_{0.05}Cu_3O_{10-\delta}$

ln $(F^{5/3}/d^3)$ for some selected samples. The calculated values of K and m are given in Table 2. The value of the exponent m can be used to identify the type of the ISE; for normal ISE $m > 0.6$, while $m < 0.6$ for the reverse ISE [46]. As noted from Table 2, the values of m lie between 0.4 and 0.47 which confirms the existence of the reverse ISE in our samples. From the analysis of data, we notice that there is a correlation between K and m as shown in Fig. 10b. The results in Fig. 10b are well fitted according to the empirical formula:

$$K = 690.72e^{12.739m}. \tag{10}$$

In order to test the applicability of the above mentioned models for our samples, the microhardness is calculated according to each model and compared with the measured H_V. Figures 11 and 12 show a comparison between the experimental H_V and the theoretical values calculated from the different models for $Cu_{0.5}Tl_{0.5}Ba_2Ca_2Cu_3O_{10-\delta}$ and $Cu_{0.5}Tl_{0.5}Ba_2Ca_{1.95}Pr_{0.05}Cu_3O_{10-\delta}$ as examples.

From the above analysis, it is concluded that Hays–Kendall approach and Elastic/Plastic deformation model cannot explain the Vickers microhardness behavior of the $Cu_{0.5}Tl_{0.5}Ba_2Ca_{2-x}Pr_xCu_3O_{10-\delta}$ samples. This is because both models based on the elastic deformation that could not observed in our case. Consequently, the theoretical microhardness calculated from both models has large deviations from the measured H_V. On the other hand, the proportional specimen resistance model is partially successful for describing the Vickers microhardness behavior of these samples. It is successful in describing the behavior of H_V with the load, while the H_V calculated from this model is much lower than that of measured. Therefore, the best model describes the Vickers microhardness of $Cu_{0.5}Tl_{0.5}Ba_2Ca_{2-x}Pr_xCu_3O_{10-\delta}$ samples is the Indentation-induced cracking (IIC) model. This conclusion is confirmed by Figs. 11 and 12 where the calculated microhardness according to IIC model is well fitted with the experimental values. The suitability of the (IIC) model to the examined samples comes from two reasons: the first one is

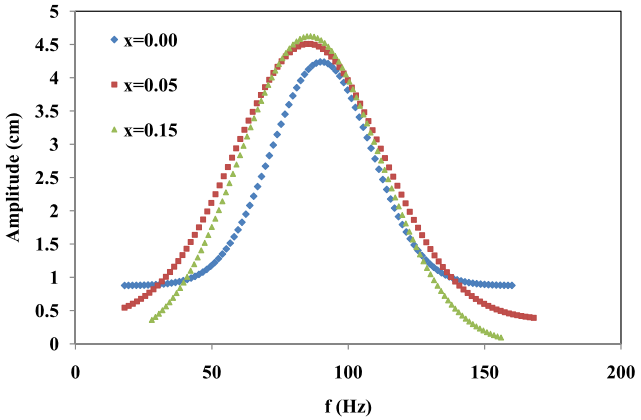

Fig. 13 Resonance curves for $Cu_{0.5}Tl_{0.5}Ba_2Ca_{2-x}Pr_xCu_3O_{10-\delta}$ with $x = 0.00$, 0.05, and 0.15

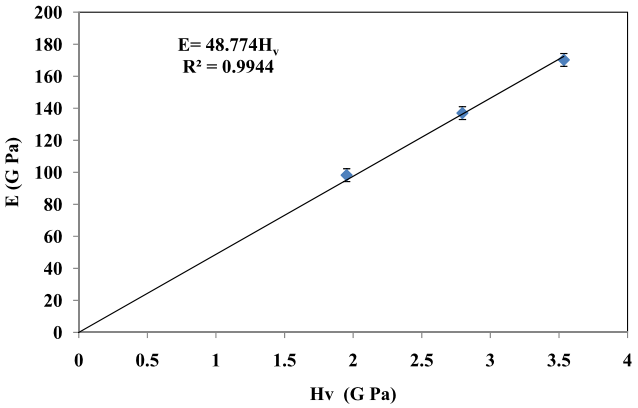

Fig. 14 The correlation between Young's modulus (E) and Vickers microhardness (H_V) for $Cu_{0.5}Tl_{0.5}Ba_2Ca_{2-x}Pr_xCu_3O_{10-\delta}$

that the specimen does not offer resistance or undergo elastic recovery as postulated in the Hays–Kendall approach, proportional specimen resistance, and elastic/plastic deformation models, but undergoes relaxation involving a release of the indentation stress away from the indentation site. This leads to a larger indentation size, and hence lower Vickers microhardness at low loads [46]. Whereas the second one is that the reverse ISE phenomenon essentially takes place in crystals which readily undergo plastic deformation, which requires that these samples are perfectly brittle and this is the case of the ceramic samples studied. The high brittleness of our samples may be attributed to the absence of the slip planes due to the strong bonding between atoms in the prepared samples.

3.3 Young's Modulus Determination

Figure 13 shows the resonance curves for $Cu_{0.5}Tl_{0.5}Ba_2Ca_{2-x}Pr_xCu_3O_{10-\delta}$ with $x = 0.00$, 0.05, and 0.15. The values of E are calculated using (2). The value of E decreases as Pr-content increases which is consistent with the Vickers microhardness results. The decreasing of E reflects the fact that E is dependent on the density of the material.

It is well known that Young's modulus is directly proportional to Vickers microhardness:

$$E \approx \text{const.} H_V. \tag{11}$$

The value of the constant of proportionality seems to be dependent on the type of the material studied. Veerender et al. [20] proposed a relation between Young's modulus and Vickers microhardness values for $Bi_{2-x}Pb_xCa_2Sr_2Cu_3O_y$, given by

$$E = 81.9635 H_V. \tag{12}$$

In order to examine the validity of this relation to our samples, the Young's modulus values determined from the dynamic resonance technique are plotted versus the Vickers microhardness values in Fig. 14. It is found that, for all samples, Young's modulus is related to the apparent Vickers microhardness by the relation:

$$E = 48.774 H_V. \tag{13}$$

This relation indicates that the dependence of E on the H_V is as that predicted, but with a new proportionality constant. This confirms that the proportionality constant depends on the structure of the studied material.

4 Conclusions

From the above analysis, the following conclusions can be drawn:

- The $(Cu_{0.5}Tl_{0.5})$-1223 superconducting phase was prepared by a single-step solid state reaction with a tetragonal unit cell. Moreover, the substitution by Pr in the Ca site does not change this crystal structure.
- $(Cu_{0.5}Tl_{0.5})$-1223 samples of a rectangular bar form exhibited reverse indentation size effect in contrary to those of a disc form [13].
- Hays–Kendall approach, elastic/plastic deformation model, and the proportional specimen resistance model failed to describe the reverse ISE for $Cu_{0.5}Tl_{0.5}Ba_2Ca_{2-x}Pr_xCu_3O_{10-\delta}$ samples.
- The dependence of Vickers microhardness for $Cu_{0.5}Tl_{0.5}Ba_2Ca_{2-x}Pr_xCu_3O_{10-\delta}$ samples on the applied load was best fitted with the indentation-induced cracking (IIC) model.
- The Pr-substitution in $(Cu_{0.5}Tl_{0.5})$-1223 reduced both Vickers microhardness and Young's modulus.
- A relation between Young's modulus and Vickers microhardness was obtained for $Cu_{0.5}Tl_{0.5}Ba_2Ca_{2-x}Pr_xCu_3O_{10-\delta}$ samples.

Acknowledgements This work was performed at the superconductivity and metallic glasses lab, Physics Department, Faculty of Science, Alexandria University, Alexandria, Egypt. Special thanks go to Prof. I.H. Ibrahim for helping in the final stage of this work. The authors thank Dr. R. Shalaby, Faculty of Science, Mansoura University for Vickers microhardness measurements.

References

1. Uzun, O., Karaaslan, T., Gogebakan, M., Keskin, M.: J. Alloys Compd. **376**, 149 (2004)
2. Kolemen, U., Uzun, O., Aksan, M.A., Guclu, N., Yakinci, E.: J. Alloys Compd. **415**, 294 (2006)
3. Kolemen, U., Uzun, O., Yilmazlar, M., Guclu, N., Yanmaz, E.: J. Alloys Compd. **415**, 300 (2006)
4. Kaur, B., Bhat, M., Licci, F., Kumar, R., Kotru, P.N., Bamzai, K.K.: Nucl. Instrum. Methods Phys. Res. **222**, 175 (2004)
5. Uzun, O., Karaaslan, T., Keskin, M.: J. Alloys Compd. **358**, 104 (2003)
6. Martinez, E., Romera, J., Lousa, A., Esteve, J.: Appl. Phys. A **77**, 419 (2003)
7. Sun, J., Francis, L.F., Gerberich, W.W.: Polym. Eng. Sci. **45**, 207 (2005)
8. Terzioglu, C., Varilci, A., Beleni, I.: J. Alloys Compd. **478**, 836 (2009)
9. Cetinkara, H.A., Yilmazar, M., Ozturk, O., Nursoy, M., Terzioglu, C.: Int. Conf. Supercond. Magn. (ICSM2008). **153**, 012038 (2009)
10. Aydin, H., Cakiroglu, O., Nursoy, M., Terzioglu, C.: Chin. J. Phys. **47**, 192 (2009)
11. Leenders, A., Ulldich, M., Freyhardt, H.C.: Physica C **279**, 173 (1997)
12. Mohammed, N.H., Abou-Aly, A.I., Ibrahim, I.H., Awad, R., Rekaby, M.: J. Alloys Compd. **486**, 733 (2009)
13. Mohammed, N.H., Abou-Aly, A.I., Ibrahim, I.H., Awad, R., Rekaby, M.: J. Supercond. Nov. Magn. (2011, in press)
14. Anshukova, N.V., Vorob'ev, G.P., Golovashkin, A.I., Ivanenko, O.M., Kozel, Z.A., Krynetskii, I.B., Levitin, R.Z., Mil', B.V., Mitsen, K.V., Snegirev, V.V.: Pisma Zh. Eksp. Teor. Fiz. **46**, 373 (1987)
15. Tarnpieri, A., Celotti, G., Guicciardi, S., Melandri, C.: Mater. Chem. Phys. **42**, 188 (1995)
16. Satoa, T., Katagirib, K., Hokaria, T., Hatakeyamaa, Y., Murakamic, A., Nyilasd, A., Kasabab, K., Teshimae, H., Hiranoe, H.: Physica C **445–448**, 422 (2006)
17. Uzuna, O., Kölemena, U., Çelebib, S., Güçlüa, N.: J. Eur. Ceram. Soc. **25**, 969 (2005)
18. Yahya, A.K., Hamid, N.A., Abd-Shukor, R., Imad, H.: Ceram. Int. **30**, 1597 (2004)
19. Khalil, S.M.: J. Phys. Chem. Solids **62**, 457 (2001)
20. Veerender, C., Dumke, V.R., Nagabhooshnam, M.: Phys. Status Solidi A **144**, 299 (1994)
21. Kiesewetter, L., Zhang, J.M., Hudeau, D., Steckenborn, A.: Sens. Actuators A, Phys. **35**, 153 (1992)
22. Kang, K., Kim, K., Lee, H.: Opt. Laser Technol. **39**, 449 (2007)
23. Akhter, N., ChulJung, H., SeobChang, H., SukKim, K.: Opt. Laser Technol. **41**, 526 (2009)
24. Voronin, G.F., Degterov, S.A.: J. Solid State Chem. **110**, 50 (1994)
25. Abou Aly, A.I., Awad, R., Kamal, M., Anas, M.: J. Low Temp. Phys. (2011). doi:10.1007/s10909-010-0339-4
26. Foerster, C.E., Lima, E., Rodrigues, P.Jr., Serbena, F.C., Lepienski, C.M., Cantão, M.P., Jurelo, A.R., Obradors, X.: Braz. J. Phys. **38**, 341 (2008)
27. Luo, J., Stevens, R.: Ceram. Int. **25**, 281 (1999)
28. Jang, B., Matsubara, H.: Mater. Lett. **59**, 3462 (2005)
29. Cho, S., de Arenas, I.B., Arenas, F.J., Ochoa, J., Ochoa, J.L.: J. Alloys Compd. **288**, 211 (1999)
30. Mott, B.W.: Microindentation Hardness Testing. Butterworths, London (1956)
31. Bückle, H.: In: Westbrook, J.H., Conrad, H. (eds.) The Science of Hardness Testing and Its Research Applications, p. 199. ASME, Metal Park (1973)
32. Bull, S.J., Page, T.F., Yoffe, E.H.: Philos. Mag. Lett. **59**, 281 (1989)
33. Li, H., Bradt, R.C.: J. Mater. Sci. **28**, 917 (1993)
34. Li, H., Han, Y.H., Bradt, R.C.: J. Mater. Sci. **29**, 5641 (1994)
35. Jain, A., Razdan, A.K., Kotru, P.N., Wanklyn, B.M.: J. Mater. Sci. **29**, 3847 (1994)
36. Tabor, D.: The Hardness of Metals. Oxford University Press, Oxford (1951)
37. Hays, C., Kendall, E.G.: Metall **6**, 275 (1973)
38. Upit, G.P., Varchenya, S.A.: Phys. Status Solidi A **17**, 831 (1966)
39. Weiss, H.J.: Phys. Status Solidi A **99**, 491 (1987)
40. Ma, Q., Clarke, D.R.: J. Mater. Res. **10**, 853 (1995)
41. Frohlich, F., Grau, P., Grellmann, W.: Phys. Status Solidi A **42**, 79 (1977)
42. Michels, B.D., Frischat, G.H.: J. Mater. Sci. **17**, 329 (1982)
43. Oliver, W.C., Hutchings, R., Pethica, J.B.: In: Blau, P.J., Lawn, B.R. (eds.) Microindentation Techniques in Materials Science and Engineering, p. 90. ASTM, Philadelphia (1986)
44. Gong, J., Wu, J., Guan, Z.: J. Eur. Ceram. Soc. **19**, 2625 (1999)
45. Li, H., Bradt, R.C.: J. Mater. Sci. **31**, 1065 (1996)
46. Sangwal, K.: Mater. Chem. Phys. **63**, 145 (2000)